

An Optimized Registration Workflow and Standard Geometric Space for Small Animal Brain Imaging

Horea-Ioan Ioanas¹ Markus Marks² Mehmet Fatih Yanik² Markus Rudin¹

¹Institute for Biomedical Engineering, ETH and University of Zurich

²Institute of Neuroinformatics, ETH and University of Zurich

Abstract — The reliability of scientific results critically depends on reproducible and transparent data processing. Cross-subject and cross-study comparability of imaging data in general, and magnetic resonance imaging (MRI) data in particular, is contingent on the quality of registration to a standard reference space. In small animal MRI this is not adequately provided by currently used processing workflows, which utilize high-level scripts optimized for human data, and adapt animal data to fit the scripts, rather than vice-versa. In this fully reproducible article we showcase a generic workflow optimized for the mouse brain, alongside a standard reference space suited to harmonize data between analysis and operation. We present four separate metrics for automated quality control (QC), and a visualization method to aid operator inspection. Benchmarking this workflow against common legacy practices reveals that it performs more consistently, better preserves variance across subjects while minimizing variance across sessions, and improves both volume and smoothness conservation RMSE approximately 3-fold. We propose this open source workflow and the QC metrics as a new standard for small animal MRI registration, ensuring workflow robustness, data comparability, and region assignment validity, important criteria for the comparability of scientific results across experiments and centers.

Background

Correspondence of brain areas across individuals is a prerequisite for making generalizable statements regarding brain function and organization. This is achieved by spatial transformation of brain maps in a study to a population or standard reference template. This process, called registration, is an integral constituent of any neuroimaging workflow attempting to produce results which are both spatially resolved and meaningful at the population level.

The computations required for registration are commonly performed at the very onset of the pre-processing workflow, though the actual image manipulation may only take place much later, once inter-

subject comparison becomes needed. As a consequence of this peripheral positioning in the pre-processing sequence, and of its general independence from experimental designs and hypotheses, registration is often relegated to default values and exempt from rigorous design efforts and QC.

Registration in human brain imaging benefits from high-level functions (e.g. `fslirt` and `fnirt` from the FSL package[1], or `antsIntroduction.sh` from the ANTs package[2]), optimized for the size and spatial features of the human brain. The availability and widespread use of such functions mitigate issues which would otherwise arise from a lack of QC. In mouse brain imaging, however, registration is frequently performed using the selfsame high-level functions from human brain imaging — rendered usable for mouse brain data by adjusting the data to fit the priors and optimized parameters of the functions, rather than vice-versa.

This general approach compromises data veracity and limits the degree to which processing can be optimized for mouse brain applications. As such, it represents a notable hurdle for the methodological improvement of mouse brain imaging.

Below, we explicitly describe current practices, in an effort to not only propose better solutions, but do so in a falsifiable manner which provides adequate detail for both the novel and the legacy methods.

Manipulations

The foremost data manipulation procedure in present-day mouse MRI is the adjustment of voxel dimensions. These dimensions are represented in the Neuroimaging Informatics Technology Initiative format (NIFTI) header [3] by affine transformation parameters, which map data matrix coordinates to geometrically meaningful spatial coordinates. Manipulations of the affine parameters are performed in order to make the data represent volumes corresponding to what human-optimized brain extraction, bias correction, and registration interfaces expect (rather than the physiological mouse brain dimensions). Com-

monly, this manipulation constitutes a 10-fold increase in each spatial dimension.

In order to produce acceptable results from brain extraction based on human priors, it may be necessary to additionally adjust the data matrix content itself. This may involve applying an ad-hoc intensity-based percentile threshold to clear non-brain or anterior/posterior brain tissue and leave a more spherical brain for the human masking functions to operate on. While conceptually superior solutions adapting parameters and priors to animal data are available [4, 5] and might remove the need for this step of data adaptation, rudimentary solutions remain popular. Both these function adaptations for animal data and the animal data matrix content adaptations for use with human brain extraction functions are, however, known to completely or partially remove the olfactory bulbs. For this reason, the choice is sometimes made to instead simply forego brain extraction.

Often, the orientation of the scan is seen as problematic, and consequently deleted. This consists in resetting the S-Form affine from the NIfTI header to zeroes, and is intended to mitigate a data orientation produced by the scanner which is incorrect with respect to the target template. While it is true that the scanner affine space reported for mouse data may be nonstandard (the confusion is two-fold: mice lie prone with the coronal plane progressing axially whereas higher primates lie supine with the horizontal plane progressing axially), the affine spaces of mouse brain templates may be nonstandard as well. A related manipulation is dimension swapping, which changes the order of the NIfTI data matrix dimensions rather than the affine metadata. Occasionally, correct or automatically redressable affine parameters are thus deleted and data is reordered beyond easy recovery, in order to correspond to a malformed template.

Templates

As the above demonstrates, the template is a key component of a registration workflow. Templates used for mouse brain MRI registration are heterogeneous and include histological, as well as ex vivo MRI templates, scanned either inside the intact skull or after physical brain extraction.

Histological templates benefit from high spatial resolution and access to molecular information in the same coordinate space. Such templates are not produced in volumetric sampling analogous to MRI, and are often not assigned a meaningful affine transformation after conversion to NIfTI. Histological contrast may only poorly correlate with any MR contrast, making registration less reliable, or necessitating the use of similarity metrics which impose additional restrictions. Not least of all, histological templates may be severely deformed and lack distal parts of the brain (such as the olfactory bulbs) due to the extraction and sampling process. Data registered to such templates may be particularly difficult to use for naviga-

tion in the intact mouse brain, e.g. during stereotactic surgery.

Ex vivo templates based on extracted brains share most of the deformation issues present in histological templates; they are, however, available in MR contrasts, making registration far easier. Ex vivo templates based on intact mouse heads provide both MR contrast and brains largely free of deformation and supporting whole brain registration. Independently of brain extraction, MR templates need to have any histological or molecular information relevant for downstream analysis first registered to them.

Challenges

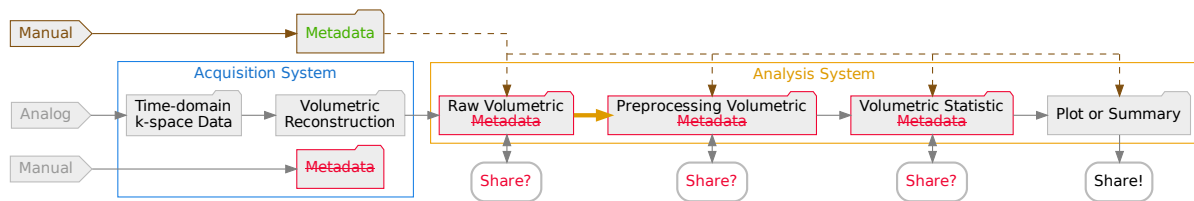
The foremost challenges in mouse MRI registration consist in eliminating data-degrading workarounds, reducing reliance on high-level interfaces with inappropriate optimizations, and reducing the number of standard space templates. Information loss (e.g. pertaining to both the affine and the data matrix) during preprocessing is a particularly besetting issue, since the loss of data at the onset of a neuroimaging workflow will persist throughout all downstream steps and preclude numerous modes of analysis (fig. 1a).

The Optimized Workflow

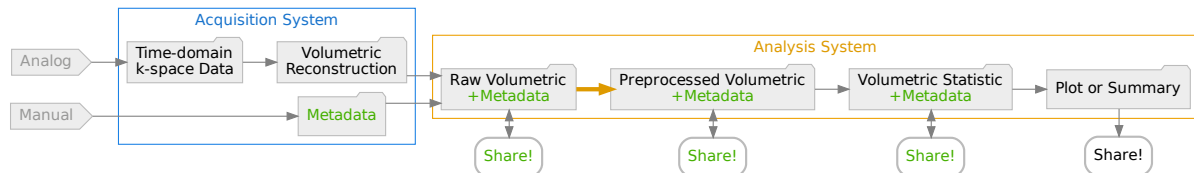
The complexity of MRI processing workflows should be manageable to prospective users with only cursory programming experience. However, workflow transparency, sustainability, and reproducibility should not be compromised for trivial features. We thus abide by the following design guidelines: (1) *each workflow is represented by a high-level function*, whose parameters correspond to operator-understandable concepts, detailing operations performed, rather than computational implementations; (2) *workflow functions are highly parameterized but include workable defaults*, so that users can change their function to a significant extent without editing the constituent code; (3) *graphical or interactive interfaces are avoided*, as they impede reproducibility, encumber the dependency graph, and reduce the sustainability of the project.

The language of choice for workflow handling is Python, owing to its Free and Open Source (FOSS) dependency stack, readability, wealth of available libraries, ease of package management, and its large and dynamic developer community. While workflow functions are written in Python, we also provide automatically generated Command Line Interfaces (CLIs) for use directly with Bash. These autogenerated CLIs ensure that features become available in Bash and Python synchronously, and workflows behave identically regardless of the invocation interface.

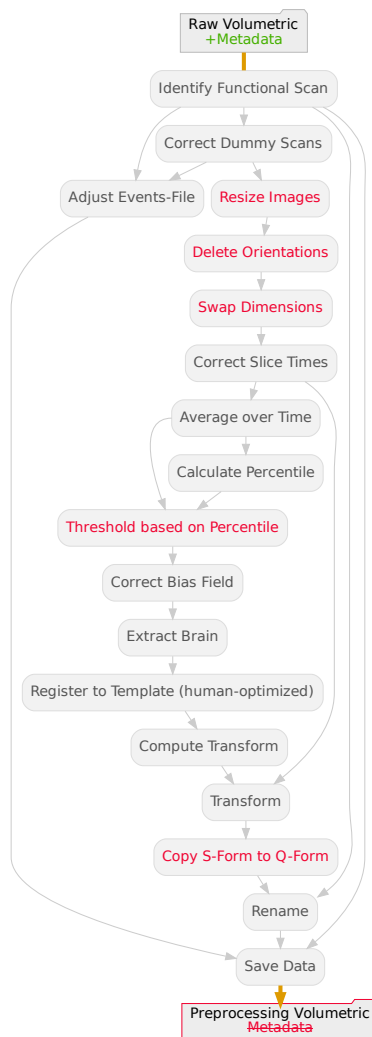
Given the aforementioned guiding principles, and the hitherto listed software choices, we have constructed two registration workflows: The novel



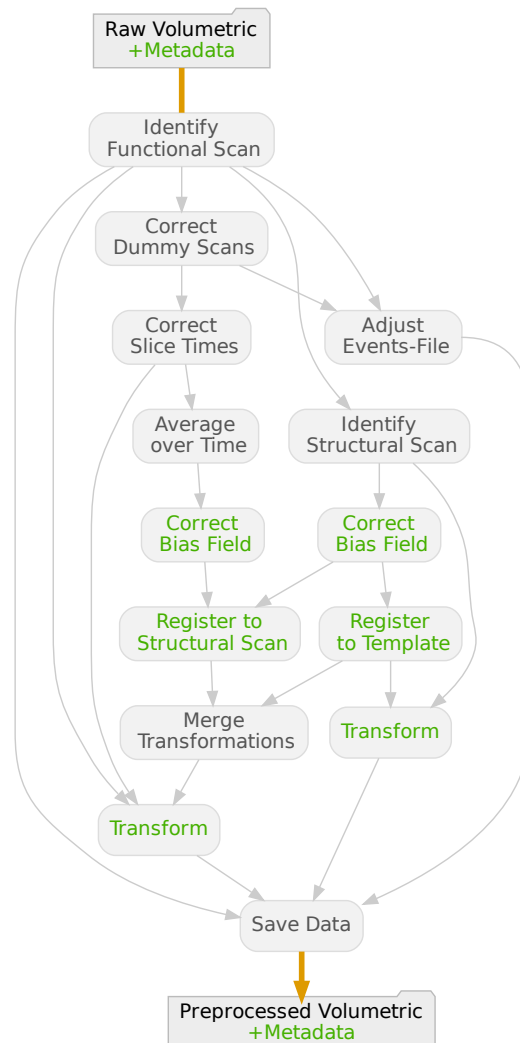
(a) Ad hoc metadata substitution irreversibly damages data and hinders reuse and sharing at all downstream levels.



(b) Nondestructive handling of metadata ensures reusability and easy sharing throughout the analysis process.



(c) "SAMRI Legacy" workflow, based on the `antsIntroduction.sh` function, and including destructive manipulations in nodes colored red.



(d) Non-destructive "SAMRI Generic" workflow, based on the `antsRegistration` function, and including mouse-specific parameter optimization in nodes colored green.

Figure 1: The SAMRI Generic workflow uses fine-tuned animal priors to enhance registration quality and preserve metadata integrity. Directed graphs depict both the overall context of MRI data processing and analysis (a,b), as well as the internal structure of the two registration workflows compared in this article (c,d), which insert into the broader context at the bold orange arrow positions. Technical detail available in fig. S3.

“Generic” workflow (fig. 1d); and the “Legacy” workflow (fig. 1c), the latter of which exhibits the common practices detailed in the Background section. Both workflows start by performing dummy scan correction on the fMRI data and the stimulation events file, based on BIDS metadata, if available. The “Legacy” workflow subsequently applies a tenfold multiplication to the voxel size (making the brain size more human-like), and deletes the orientation information from the affine matrix. Further, the dimensions are swapped so that the data matrix matches the RPS (left→Right, anterior→Posterior, inferior→Superior) orientation of the corresponding template (see fig. 2b). Following these data manipulation steps, a temporal mean is computed, and an empirically determined signal threshold (10 % of the 98th percentile) is applied. Subsequently, the bias field is corrected using the `fast` function of the FSL package, and parts of the image are masked using the `bet` function from FSL. The image is then warped into the template space using the `antsIntroduction.sh` function of the ANTs package. Lastly, the affine variants are harmonized. The “Generic” workflow follows up on dummy scan correction with slice timing correction, computes the temporal mean of the functional scan (to obtain a more representative contrast for the whole time course), and applies a bias field correction to the temporal mean — using the `N4BiasFieldCorrection` function of the ANTs package, with spatial parameters adapted to the mouse brain. Analogous operations are performed on the structural scan, following which the structural scan is registered to the reference template, and the functional scan temporal mean is registered to the structural scan — using the `antsRegistration` function of the ANTs package, with spatial parameters adapted to the mouse brain. The structural-to-template and functional-to-structural transformation matrices are then merged, and applied in one warp computation step to the functional data — while the structural data is warped solely based on the structural-to-template transformation matrix.

For Quality Control we distribute as part of this publication additional workflows using the NumPy [6], SciPy [7], pandas [8], and matplotlib packages [9], as well as Seaborn [10] for plotting, and Statsmodels [11] for top-level statistics, using the HC3 heteroscedasticity consistent covariance matrix [12]. Specifically, distribution densities for plots are drawn using the Scott bandwidth density estimator [13].

Distribution

As registration is a crucial step of a larger data analysis process (rather than an analysis process in its own right), the workflows are best distributed as part of a comprehensive workflow package. We include the aforementioned Generic and Legacy workflows in the SAMRI (Small Animal Magnetic Resonance Imaging) data analysis package [14] of the ETH/UZH Institute for Biomedical Engineering.

Template Package

The suitability of a registration workflow as a standard is contingent on the quality of the template being used. Particularly the size and orientation of the template may impose constraints on the workflow. For example, an unrealistically inflated template size mandates according parameters for all functions which deal with the data in its affine space. Additionally, if the template axis orientation deviates by more than 45° from the image to be registered, or if an axis is flipped, the global maximum of the first (rigid) registration step may not be correctly determined, and the image would then be skewed and nonlinearly deformed to match the template at an incorrect orientation. Consequently, template quality needs to be ascertained, and a workflow-compliant default should be provided.

Our recommended template (fig. 2a) is derived from the DSURQE template of the Toronto Hospital for Sick Children Mouse Imaging Center [15]. The geometric origin of this template is shifted to match the Bregma landmark, and thus provide integration with histological atlases and surgical procedures, which commonly use Bregma as a reference. The template is in the canonical orientation of the NIFTI format, RAS (left→Right, posterior→Anterior, inferior→Superior), and has a coronal slice positioning reflective of both the typical animal head position in MR scanners and in stereotactic surgery frames. The template is provided at 40 µm and 200 µm isotropic resolutions, and all of its associated mask and label files are identified with the prefix `dsurqec` in the template packages.

We bundle the aforementioned MR template with two additional histological templates, derived from the Australian Mouse Brain Mapping Consortium (AMBMC) [16], and the Allen Brain Institute (ABI) [17] templates. While these suffer from shortcomings listed under the Background section, we include the AMBMC template due to its extra long rostrocaudal coverage, and the ABI atlas due to its role as the reference atlas for numerous gene expression and projection maps. We reorient the AMBMC template from its original RPS orientation to the canonical RAS, and apply an RAS orientation to the orientation-less ABI template after converting it to NIFTI from its original NRRD format. These templates are also made available at 40 µm and 200 µm isotropic resolutions, and the corresponding files are prefixed with `ambmc` and `abi`, respectively.

Additionally, we provide templates in the historically prevalent but incorrect, RPS orientation, and with the historically prevalent tenfold increase in voxel size. These templates are derived from the DSURQE and AMBMC templates, and are prefixed with `ldsurque` and `lambmc`, respectively.

Lastly, due to data size considerations, we distribute 15 µm isotropic versions of all tem-

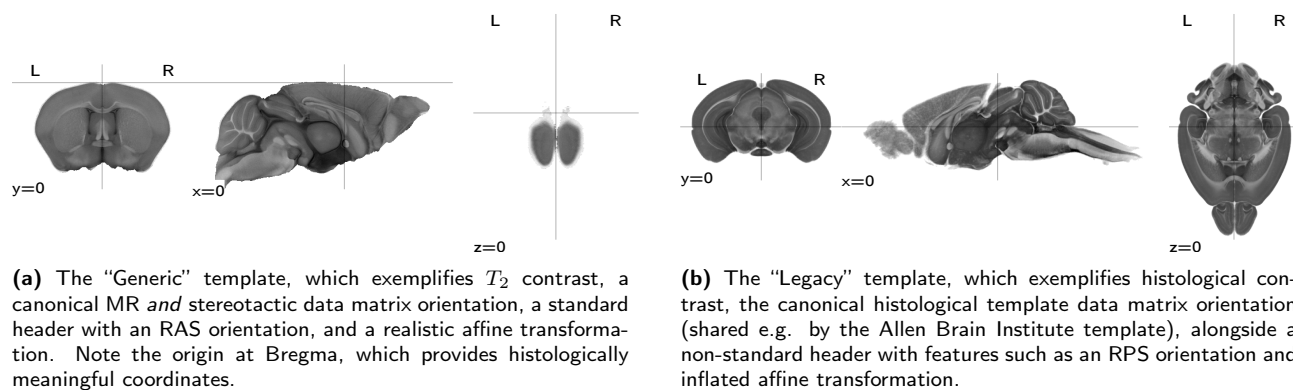


Figure 2: The "Generic" template provides canonical orientation and Bregma centering. Illustrated are multiplanar depictions of the "Generic" and "Legacy" mouse brain templates, with slice coordinates centered at zero on all axes.

plates available at this resolution (AMBMC and its legacy derivative, as well as ABI) in a separate package. The two packages we thus distribute are called `mouse-brain-atlases` and `mouse-brain-atlasesHD`. Up-to-date versions of these archives can be reproduced via a FOSS script collection which handles download, reorienting, and resampling, and was written and released for the purpose of this publication [18].

For the comparisons performed in this text, the `dsurqec` and `ldsurgec` template variations (containing the same data matrix, but matched to the orientation and size requirements of the functions in the fig. 1d and fig. 1c workflows, respectively) are referred to as the "Generic" template. Analogously, the `ambmc` and `lambmc` template variations are referred to as the "Legacy" template.

Interactive Operator Inspection

We complement the automated whole-dataset evaluation metrics detailed at length in this article with convenience functions to ease and improve interactive operator inspection. These functions produce clean, well-paginated, and visually pleasing slice-by-slice views of the registered data, and emphasize one of two different quality assessments. The first view mode highlights single-session registration quality by plotting the registered data as a greyscale bitmap, and the target atlas as a coloured contour (figs. S1a to S1d). The second view mode highlights multi-session registration coherence, by plotting the target template as a greyscale bitmap, and the individual session percentile contours in colour (fig. S2).

Reproducibility

The source code for this document and all data analysis shown herein (including registration and QC workflow execution) is published according to the RepSeP specifications [19]. The data analysis execution and document compilation has been tested repeatedly on numerous hardware platforms, with operating systems including Gentoo Linux and MacOS, and as such

we attest that all figures and statistics presented can be reproduced based solely on the raw data, dependency list, and analysis scripts which we distribute.

Evaluation

A major challenge of registration QC is that a perfect mapping from the measured image to the template is undefined. Similarity metrics are ill-suited for QC because they are used internally by registration functions, whose mode of operation is based on maximizing them. Extreme similarity score maximization is not a desired outcome, particularly if nonlinear transformations are employed, as this may result in image distortions which should be penalized in QC. Moreover, similarity metrics are not independent, so the issues arising from similarity score maximization cannot be circumvented by maximizing a subset of metrics and performing QC via the remainder. To address this challenge, we developed four alternative evaluation metrics: volume conservation, smoothness conservation, functional analysis, and variance analysis. In order to mitigate possible differences arising from template features, we use these metrics for multi-factorial analyses — including both a template and a workflow factor.

Volume Conservation

Volume conservation is based on the assumption that the total volume of the scanned segment of the brain should remain roughly constant after preprocessing. Beyond just size differences between the acquired data and the target template, a volume increase may indicate that the brain was stretched to fill in template brain space not covered by the scan, while a volume decrease might indicate that non-brain voxels were introduced into the template brain space. For this analysis we compute a Volume Conservation Factor (VCF), whereby volume conservation is highest for a VCF equal to 1.

As seen in fig. 3a, we note that in the described dataset VCF is sensitive to the workflow ($F_{1,268} =$

173.2, $p = 7.49 \times 10^{-31}$), the template ($F_{1,268} = 530.9$, $p = 1.62 \times 10^{-65}$), but not the interaction thereof ($F_{1,268} = 3.264$, $p = 0.072$).

The performance of the Generic SAMRI workflow in conjunction with the Generic template is significantly different from that of the Legacy workflow in conjunction with the Legacy template, yielding a two-tailed p-value of 2.6×10^{-12} . Moreover, the root mean squared error ratio strongly favours the Generic workflow ($\text{RMSE}_L/\text{RMSE}_G \simeq 2.9$).

Descriptively, we observe that the Legacy level of the template variable introduces a notable volume loss (VCF of -0.34 , 95%CI: -0.37 to -0.32), while the Legacy level of the workflow variable introduces a volume gain (VCF of 0.20 , 95%CI: 0.17 to 0.22). Further, we note that there is a very strong variance increase in all conditions for the Legacy workflow (22-fold given the Legacy template, and 5.1-fold given the Generic template).

With respect to the data break-up by contrast (CBV versus BOLD, fig. 3b), we see no notable main effect for the contrast variable (VCF of -0.02 , 95%CI: -0.05 to 0.01). We do, however, report a notable effect for the contrast-template interaction, with the Legacy workflow and CBV contrast interaction level introducing a volume loss (VCF of -0.16 , 95%CI: -0.19 to -0.13).

Smoothness Conservation

A further aspect of preprocessing quality is the resulting image smoothness. Although controlled smoothing is a valuable preprocessing tool used to increase the signal-to-noise ratio (SNR), uncontrolled smoothness limits operator discretion in the trade-off between SNR and feature granularity. Uncontrolled smoothness can thus lead to undocumented and implicit loss of spatial resolution and is therefore associated with inferior anatomical alignment [20]. We employ a Smoothness Conservation Factor (SCF), expressing the ratio between the smoothness of the preprocessed images and the smoothness of the original images.

With respect to the data shown in fig. 3c, we note that SCF is sensitive to the template ($F_{1,268} = 60.54$, $p = 1.56 \times 10^{-13}$), the workflow ($F_{1,268} = 433$, $p = 6.77 \times 10^{-58}$), and the interaction of the factors ($F_{1,268} = 9.103$, $p = 0.0028$).

The performance of the Generic SAMRI workflow in conjunction with the Generic template is significantly different from that of the Legacy workflow in conjunction with the Legacy template, yielding a two-tailed p-value of 1.1×10^{-23} . In this comparison, the root mean squared error ratio favours the Generic workflow ($\text{RMSE}_L/\text{RMSE}_G \simeq 2.9$).

Descriptively, we observe that the Legacy level of the template variable introduces a smoothness reduction (SCF of -0.14 , 95%CI: -0.16 to -0.11), while the Legacy level of the workflow variable introduces a smoothness gain (SCF of 0.36 , 95%CI: 0.34 to 0.39). Further, we note that there is a strong variance in-

crease for the Legacy workflow (4.92-fold given the Legacy template and 4.69-fold given the Generic template).

Given the break-up by contrast shown in fig. 3d, we see only very weak effect sizes for the contrast variable (SCF of 0.06 , 95%CI: 0.01 to 0.10) and the contrast-template interaction (SCF of 0.04 , 95%CI: 0.00 to 0.08).

Functional Analysis

Functional analysis is a frequently used avenue for preprocessing QC. Its viability derives from the fact that the metric being maximized in the registration process is not the same output metric as that used for QC. The method is however primarily suited to examine workflow effects in light of higher-level applications, and less suited for wide-spread QC (as it is computationally intensive and only applicable to stimulus-evoked functional data). Additionally, functional analysis significance is documented to be sensitive to data smoothness [21], and thus an increased score on account of uncontrolled smoothing can be expected. For this analysis we compute the Mean Significance (MS), expressing the significance detected across all voxels of a scan.

As seen in fig. 3e, MS is sensitive to the workflow ($F_{1,268} = 4.838$, $p = 0.029$), but not to the template ($F_{1,268} = 0.046$, $p = 0.83$), nor the interaction of both factors ($F_{1,268} = 0.063$, $p = 0.8$).

The performance of the SAMRI Generic workflow (with the Generic template) differs significantly from that of the Legacy workflow (with the Legacy template) in terms of MS, yielding a two-tailed p-value of 1.5×10^{-8} .

Descriptively, we observe that the Legacy level of the workflow variable introduces a notable significance increase (MS of 0.78 , 95%CI: 0.60 to 0.97), while the Legacy level of the template variable (MS of -0.08 , 95%CI: -0.27 to 0.11), and the interaction of the Legacy template and Legacy workflow (MS of -0.13 , 95%CI: -0.39 to 0.14) introduce no significance change. Furthermore, we again note a variance increase in all conditions for the Legacy workflow (2.4-fold given the Legacy template, and 2.6-fold given the Generic template).

With respect to the data break-up by contrast (fig. 3f), we see no notable main effect for the contrast variable (MS of -0.09 , 95%CI: -1.05 to 0.88) and no notable effect for the contrast-template interaction (MS of -0.30 , 95%CI: -0.65 to 0.05).

Functional analysis effects can further be inspected by visualizing the statistic maps. Second-level t-statistic maps depicting the CBV and BOLD omnibus contrasts (common to all subjects and sessions) provide a succinct overview capturing both amplitude and directionality of the signal (fig. 4). Crucial to the examination of registration quality and its effects on functional read-outs is the differential coverage. We note that the Legacy workflow in-

duces coverage overflow, extending to the cerebellum (figs. 4c, 4d, 4g and 4h), as well as to more rostral areas when used in conjunction with the Legacy template (figs. 4d and 4h). Separately from the Legacy workflow, the Legacy template causes acquisition slice misalignment (figs. 4b, 4d and 4h). Positive activation of the Raphe system, most clearly disambiguated from the surrounding tissue in the BOLD contrast, is notably displaced very far caudally by the joint effects of the Legacy workflow and the Legacy template (fig. 4h). We note that processing with the Generic template and workflow (figs. 4a and 4e), does not show issues with statistic coverage alignment and overflow.

Variance Analysis

An additional way to assess preprocessing quality focuses on the robustness to variability across repeated measurements, and whether this is attained without overfitting (i.e. compromising physiologically meaningful variability). The core assumption of this analysis of variance is that adult mouse brains in the absence of intervention retain size, shape, and implant position throughout the 8 week study period. Consequently, when examining similarity scores of preprocessed scans with respect to the target template, more variation should be found across levels of the subject variable rather than session variable. This comparison can be performed using a type 3 ANOVA, modelling both the subject and the session variables. For this assessment we select three metrics with maximal sensitivity to different features: Neighborhood Cross Correlation (CC, sensitive to localized correlation), Global Correlation (GC, sensitive to whole-image correlation), and Mutual Information (MI, sensitive to whole-image information similarity).

Figure 5 renders the similarity metric scores for both the SAMRI Generic and Legacy workflows (considering only the matching workflow-template combinations). The Legacy workflow produces results which show a higher F-statistic for the session than for the subject variable: CC (subject: $F_{10,19}=0.068$, $p=1$, session: $F_{4,19}=0.38$, $p=0.82$), GC (subject: $F_{10,19}=0.7$, $p=0.72$, session: $F_{4,19}=3.11$, $p=0.04$), and MI (subject: $F_{10,19}=1.769$, $p=0.14$, session: $F_{4,19}=3.206$, $p=0.036$).

The Generic SAMRI workflow shows a reversing trend. Resulting data F-statistics are consistently higher for the subject variable than for the session variable: CC (subject: $F_{10,19}=5.27$, $p=0.00095$, session: $F_{4,19}=3.112$, $p=0.04$), GC (subject: $F_{10,19}=2.588$, $p=0.036$, session: $F_{4,19}=1.795$, $p=0.17$), and MI (subject: $F_{10,19}=1.772$, $p=0.14$, session: $F_{4,19}=1.578$, $p=0.22$).

Discussion

The workflow and template design presented herein offer significant advantages in terms of reducing cov-

erage overestimation, uncontrolled smoothness, and guaranteeing session-to-session consistency. This is most clearly highlighted by Volume Conservation (fig. 3a), Smoothness Conservation (fig. 3c), and Variance Analysis (fig. 5), where the combined usage of the SAMRI Generic workflow and template outperforms all other combinations of the multi-factorial analysis. Increased region assignment validity is also revealed in a qualitative examination of higher-level functional maps (fig. 4), where only the combination of the Generic workflow and template provides accurate coverage of the sampled volume for both BOLD and CBV fMRI data. These benefits are robust to the functional contrast (figs. 3b, 3d and 3f), with the Generic workflow-template combination being less or equally susceptible to the contrast variable, when compared to the Legacy workflow-template combination. The performance of the Generic workflow is more consistent across all metrics, as demonstrated by notable reductions of the standard deviation for both VCS, SCF, as well as MS (figs. 3a, 3c and 3e).

Closer model inspection reveals that in addition to the processing factor, the template factor is also a strong source of variability. The Legacy template induces both a volume and a smoothness decrease beyond the original data values (figs. 3a and 3c). This clearly indicates a whole-volume effect, whereby a target template smaller than the recoded brain size causes a contraction of the brain during registration, resulting both in a volume and a smoothness loss. This effect can also be observed qualitatively in fig. 4. We thus highlight the importance of an appropriate template choice, and strongly recommend usage of the Generic template on account of its better scale similarity to data acquired in adult mice.

The volume conservation, smoothness conservation, and session-to-session consistency of the SAMRI Generic workflow and template combination are further augmented by numerous design benefits (figs. 1 and 2). These include increased transparency and parameterization of the workflow (which can more easily be inspected and further improved or customized), veracity of resulting data headers, and spatial coordinates more meaningful for surgery and histology.

Quality Control

A major contribution of this work is the implementation of multiple metrics providing simple, powerful and robust QC for registration performance (VCF, SCF, MS, and Variance Analysis) and the release of a dataset [22] suitable for such multifaceted benchmarking — including the analysis of session-wise and subject-wise variability.

The VCF and SCF provide good quantitative estimates of distortion prevalence. The analysis comparing subject-wise and session-wise variance is an elegant avenue allowing the operator to ascertain how much a registration workflow is potentially overfitting, by differentiating between meaningful (inter-subject)

and confounding (inter-session) variability. These metrics are relevant to both preclinical and clinical MRI workflow improvements, and could themselves be further optimized.

Global statistical power is not a reliable metric for registration optimization. Regrettably, however, it may be the most prevalently used if results are only inspected at a higher level — and could bias analysis. This is exemplified by the positive main effect of the Legacy workflow seen in fig. 3e. In this particular case, optimizing for statistical power alone would give a misleading indication, as becomes evident when all other metrics are inspected.

We suggest that a VCF, SCF and Variance based comparison, coupled with visual inspection of a small number of omnibus statistic maps is a feasible and sufficient tool for benchmarking workflows. We recommend reuse of the presented data for workflow benchmarking, as they include (a) multiple sources of variation (contrast, session, subjects), (b) functional activity with broad coverage but spatially distinct features, and (c) significant distortions due to implant properties — which are appropriate for testing workflow robustness. In addition to the workflow code [14], we openly release the re-executable source code [23] for all statistics and figures in this document. It is thus not just the novel method, but also the benchmarking process which is fully transparent and reusable with further data.

Conclusion

We present a novel registration workflow, entitled SAMRI Generic, which offers several advantages compared to the ad hoc approaches commonly used for small animal MRI. In depth multivariate comparison with a thoroughly documented Legacy pipeline revealed superior performance of the SAMRI Generic workflow in terms of volume and smoothness conservation, as well as variance structure across subjects and sessions. The metrics introduced for registration QC are not restricted to the processing of small animal fMRI data, but can be readily expanded to other brain imaging applications. The optimized registration parameters of the SAMRI Generic Workflow are easily accessible in the source code and transferable to any other workflows making use of the ANTs package. The open source software choices in both the workflow and this article's source code empower users to better verify, understand, remix, and reuse our work. Overall, we believe that using the SAMRI Generic workflow should facilitate and harmonize processing of mouse brain imaging data across studies and centers.

Methods

For the quality control of the workflows, a dataset with an effective size of 102 scans is used. Data from

11 adult animals (6 males and 5 females, 207 days to 261 days old at study onset) is included, with each animal scanned on up to 5 sessions (repeated at 14 day intervals). Each session contains an anatomical scan and two functional scans — with Blood-Oxygen Level Dependent (BOLD) [24] and Cerebral Blood Volume (CBV) [25] contrast, respectively (for a total of 68 functional scans).

Anatomical scans were acquired via a TurboRARE sequence, with a RARE factor of 8, an echo time (TE) of 21 ms, an inter-echo spacing of 7 ms, and a repetition time (TR) of 2500 ms, sampled at a sagittal resolution of $\Delta x(\nu) = 166.7 \mu\text{m}$, a horizontal resolution of $\Delta y(\phi) = 75 \mu\text{m}$, and a coronal resolution of $\Delta z(t) = 650 \mu\text{m}$ (slice thickness of 500 μm). The field of view covered $20 \times 9 \text{ mm}^2$ and was sampled via a 120×120 matrix. A total of 14 slices were acquired.

The functional BOLD and CBV scans were acquired using a gradient-echo Echo Planar Imaging (ge-EPI) sequence with a flip angle of 60° and with TR/TE = 1000 ms/15 ms and TR/TE = 1000 ms/5.5 ms, respectively. Functional scans were sampled at $\Delta x(\nu) = 312.5 \mu\text{m}$, $\Delta y(\phi) = 281.25 \mu\text{m}$, and $\Delta z(t) = 650 \mu\text{m}$ (slice thickness of 500 μm). The field of view covered $20 \times 9 \text{ mm}^2$ and was sampled via a 64×32 matrix. A total of 14 slices were acquired.

All aforementioned scans were acquired with a Bruker PharmaScan system (7 T, 16 cm bore), and an in-house T/R coil.

The measured animals were fitted with an optic fiber implant ($l = 3.2 \text{ mm}$ $d = 400 \mu\text{m}$) targeting the Dorsal Raphe (DR) nucleus in the brain stem. The nucleus was rendered sensitive to optical stimulation by transgenic expression of Cre recombinase under the ePet promoter [26] and viral injection of rAAVs delivering a plasmid with Cre-conditional expression of Channelrhodopsin and YFP — pAAV-EF1a-double floxed-hChR2(H134R)-EYFP-WPRE-HGHpA, a gift from Karl Deisseroth (Addgene plasmid #20298).

The DR was stimulated via an Omicron LuxX 488-60 laser (488 nm) tuned to 30 mW at contact with the fiber implant, according to the protocol listed in table S1. The operation and stimulation procedure, as well as general picture of obtained activation is consistent with previous results [27], and is not further commented in this study.

All experimental procedures were approved by the Veterinary Office of the Canton of Zurich and done in accordance with the relevant regulations.

Metrics

For the current VCF implementation we define brain volume as estimated by the 66th voxel intensity percentile of the raw scan before any processing. The arbitrary unit equivalent of this percentile threshold is recorded for each scan and applied to all preprocessing workflow results for that particular scan, to obtain VCF estimates — eq. (1), where v is the voxel

volume in the original space, v' the voxel volume in the transformed space, n the number of voxels in the original space, m the number of voxels in the transformed space, s a voxel value sampled from the vector S containing all values in the original data, and s' a voxel value sampled from the transformed data.

$$VCF = \frac{v' \sum_{i=1}^m [s'_i \geq P_{66}(S)]}{v \sum_{i=1}^n [s_i \geq P_{66}(S)]} = \frac{v' \sum_{i=1}^m [s'_i \geq P_{66}(S)]}{v[0.66n]} \quad (1)$$

The SCF metric is based on the ratio of smoothness before and after processing. The smoothness measure is the full-width at half-maximum (FWHM) of the signal amplitude spatial autocorrelation function (ACF [28]). Since fMRI data usually do not have a Gaussian-shaped spatial ACF, we use AFNI [29] to fit the following function in order to compute the FWHM — eq. (2), where r is the distance of two amplitude distribution samples, a is the relative weight of the Gaussian term in the model, b is the width of the Gaussian and c the decay of the mono-exponential term [30].

$$ACF(r) = a * e^{-r^2/(2*b^2)} + (1 - a) + e^{-r/c} \quad (2)$$

We examine statistical power as relevant for the MS metric via the negative logarithm of first-level p-value maps. This produces voxelwise statistical estimates for the probability that a time course could — by chance alone — be at least as well correlated with the stimulation regressor as the voxel time course measured. We compute the per-scan average of these values as seen in eq. (3), where n represents the number of statistical estimates in the scan, and p is a p-value.

$$MS = \frac{\sum_{i=1}^n -\log(p_i)}{n} \quad (3)$$

Software

The workflow functions make use of the Nipype [31] package, which provides high-level workflow management and execution features. Via this package, functions provided by any other package can be encapsulated in a node (complete with error reporting and isolated re-execution support) and integrated into a directed workflow graph. Parallelization can also be managed via a number of execution plugins, allowing scalability. Most importantly, Nipype can generate graph descriptor language (DOT) summaries, as well as visual workflow representations suitable for operator inspection, graph theoretical analysis, and programmatic comparison between workflow variants.

Via Nipype, we utilize basic MRI preprocessing functions from the FSL package [1] and registration functions from the ANTs package [2]. While there is theoretically no limit to the number of external packages usable with Nipype, we constrain our choice as much as possible in order to minimize the dependency

graph. The choice of the ANTs package (in addition to FSL, which also provides registration functions) owes to the package's functions being more highly parameterized. This feature allows us to avoid maladaptive optimization choices, and instead fine-tune the registration to the overarching characteristics of the brain type at hand. Additionally, we have implemented a number of functions in our workflow directly, e.g. to read BIDS [32] inputs, and perform dummy scans management.

For Quality Control we distribute as part of this publication additional workflows using the NumPy [6], SciPy [7], pandas [8], and matplotlib packages [9], as well as Seaborn [10] for plotting, and Statsmodels [11] for top-level statistics, using the HC3 heteroscedasticity consistent covariance matrix [12]. Specifically, distribution densities for plots are drawn using the Scott bandwidth density estimator [13].

Data and Code Availability

The data archive relevant for this article is freely available [22], and automatically accessible via the Gentoo Linux package manager. The code relevant for reproducing this document is also freely available [23], as are its dependencies, and most prominently, SAMRI [14], the package via which the herein described workflows are distributed.

References

- [1] Mark Jenkinson, Christian F. Beckmann, Timothy E. J. Behrens, Mark W. Woolrich, and Stephen M. Smith. FSL. *Neuroimage*, 62(2):782–790, August 2012. doi: 10.1016/j.neuroimage.2011.09.015. URL <http://dx.doi.org/10.1016/j.neuroimage.2011.09.015>.
- [2] Brian B. Avants, Nicholas J. Tustison, Gang Song, Philip A. Cook, Arno Klein, and James C. Gee. A reproducible evaluation of ANTs similarity metric performance in brain image registration. *NeuroImage*, 54(3):2033–2044, February 2011. doi: 10.1016/j.neuroimage.2010.09.025. URL <https://doi.org/10.1016/j.neuroimage.2010.09.025>.
- [3] Robert W Cox, John Ashburner, Hester Berman, Kate Fissell, Christian Haselgrove, Colin J Holmes, Jack L Lancaster, David E Rex, Stephen M Smith, Jeffrey B Woodward, and Stephen C Strother. A (Sort of) New Image Data Format Standard: NIfTI-1. In *OHBM*, June 2004.
- [4] Tobias Wood, David Lythgoe, and Steven Williams. rBET: Making BET work for Rodent Brains. In *Proceedings of the ISMRM*, page 2706, April 2013.

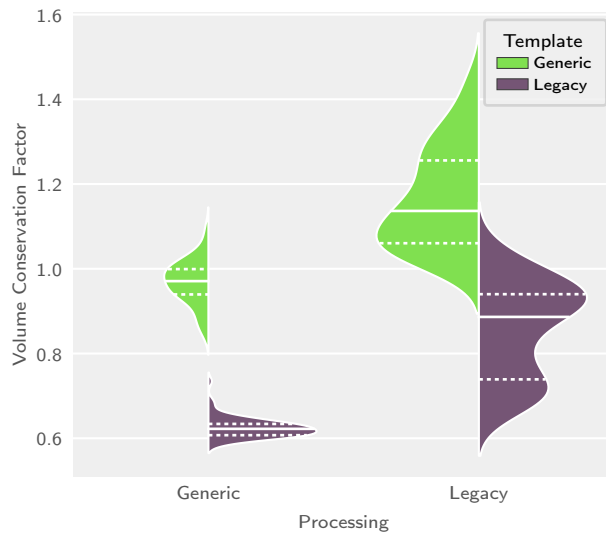
- [5] Ipek Oguz, Honghai Zhang, Ashley Rumble, and Milan Sonka. RATS: Rapid Automatic Tissue Segmentation in rodent brain MRI. *Journal of Neuroscience Methods*, 221:175–182, January 2014. doi: 10.1016/j.jneumeth.2013.09.021. URL <https://doi.org/10.1016/j.jneumeth.2013.09.021>.
- [6] Travis E. Oliphant. *Guide to NumPy*. Provo, UT, March 2006. URL <https://www.numpy.org/devdocs/contents.html>.
- [7] K. Jarrod Millman and Michael Aivazis. Python for scientists and engineers. *Computing in Science & Engineering*, 13(2):9–12, March 2011. doi: 10.1109/mcse.2011.36. URL <https://doi.org/10.1109/mcse.2011.36>.
- [8] Wes McKinney. Data Structures for Statistical Computing in Python. In Stéfan van der Walt and Jarrod Millman, editors, *Proceedings of the 9th Python in Science Conference*, pages 51 – 56, June 2010.
- [9] John D. Hunter. Matplotlib: A 2D Graphics Environment. *Computing in Science & Engineering*, 9(3):90–95, June 2007. doi: 10.1109/mcse.2007.55. URL <https://doi.org/10.1109/mcse.2007.55>.
- [10] Michael Waskom, Olga Botvinnik, Drew O’Kane, Paul Hobson, Saulius Lukauskas, David C Gempertine, Tom Augspurger, Yaroslav Halchenko, John B. Cole, Jordi Warmerhoven, Julian de Ruiter, Cameron Pye, Stephan Hoyer, Jake Vanderplas, Santi Villalba, Gero Kunter, Eric Quintero, Pete Bachant, Marcel Martin, Kyle Meyer, Alistair Miles, Yoav Ram, Tal Yarkoni, Mike Lee Williams, Constantine Evans, Clark Fitzgerald, Brian, Chris Fonnesbeck, Antony Lee, and Adel Qalieh. Seaborn: v0.8.1, September 2017. URL <https://doi.org/10.5281/zenodo.883859>.
- [11] Skipper Seabold and Josef Perktold. Statsmodels: Econometric and statistical modeling with Python. In *9th Python in Science Conference*, June 2010. URL <http://conference.scipy.org/proceedings/scipy2010/pdfs/seabold.pdf>.
- [12] J Scott Long and Laurie H Ervin. Using heteroscedasticity consistent standard errors in the linear regression model. *The American Statistician*, 54(3):217–224, August 2000. doi: 10.2307/2685594. URL <https://www.jstor.org/stable/2685594>.
- [13] David W. Scott. On optimal and data-based histograms. *Biometrika*, 66(3):605–610, December 1979. doi: 10.1093/biomet/66.3.605. URL <https://doi.org/10.1093/biomet/66.3.605>.
- [14] Horea-Ioan Ioanas, Markus Marks, Dominik Schmidt, Florian Aymanns, and Markus Rudin. SAMRI — Small Animal Magnetic Resonance Imaging, November 2017. URL <https://doi.org/10.5281/zenodo.1044033>.
- [15] A.E. Dorr, J.P. Lerch, S. Spring, N. Kabani, and R.M. Henkelman. High resolution three-dimensional brain atlas using an average magnetic resonance image of 40 adult c57bl/6j mice. *NeuroImage*, 42(1):60–69, August 2008. doi: 10.1016/j.neuroimage.2008.03.037. URL <https://doi.org/10.1016/j.neuroimage.2008.03.037>.
- [16] Andrew L. Janke and Jeremy F.P. Ullmann. Robust methods to create ex vivo minimum deformation atlases for brain mapping. *Methods*, 73:18–26, February 2015. doi: 10.1016/j.ymeth.2015.01.005. URL <https://doi.org/10.1016/j.ymeth.2015.01.005>.
- [17] Ed S. Lein, Michael J. Hawrylycz, Nancy Ao, Mikael Ayres, Amy Bensinger, Amy Bernard, Andrew F. Boe, Mark S. Boguski, Kevin S. Brockway, Emi J. Byrnes, Lin Chen, Li Chen, Tsuey-Ming Chen, Mei Chi Chin, Jimmy Chong, Brian E. Crook, Aneta Czaplinska, Chinh N. Dang, Suvro Datta, Nick R. Dee, Aimee L. Desaki, Tsega Desta, Ellen Diep, Tim A. Dolbeare, Matthew J. Donelan, Hong-Wei Dong, Jennifer G. Dougherty, Ben J. Duncan, Amanda J. Ebbert, Gregor Eichele, Lili K. Estin, Casey Faber, Benjamin A. Facer, Rick Fields, Shanna R. Fischer, Tim P. Fliss, Cliff Frensley, Sabrina N. Gates, Katie J. Glatfelter, Kevin R. Halverson, Matthew R. Hart, John G. Hohmann, Maureen P. Howell, Darren P. Jeung, Rebecca A. Johnson, Patrick T. Karr, Reena Kawal, Jolene M. Kidney, Rachel H. Knapik, Chihchau L. Kuan, James H. Lake, Annabel R. Laramée, Kirk D. Larsen, Christopher Lau, Tracy A. Lemon, Agnes J. Liang, Ying Liu, Lon T. Luong, Jesse Michaels, Judith J. Morgan, Rebecca J. Morgan, Marty T. Mortrud, Nerick F. Mosqueda, Lydia L. Ng, Randy Ng, Geralyn J. Orta, Caroline C. Overly, Tu H. Pak, Sheana E. Parry, Sayan D. Pathak, Owen C. Pearson, Ralph B. Puchalski, Zackery L. Riley, Hannah R. Rockett, Stephen A. Rowland, Joshua J. Royall, Marcos J. Ruiz, Nadia R. Sarno, Katherine Schaffnit, Nadiya V. Shapovalova, Taz Sivasay, Clifford R. Slaughterbeck, Simon C. Smith, Kimberly A. Smith, Bryan I. Smith, Andy J. Sodt, Nick N. Stewart, Kenda-Ruth Stumpf, Susan M. Sunkin, Madhavi Sutram, Angelene Tam, Carey D. Teemer, Christina Thaller, Carol L. Thompson, Lee R. Varnam, Axel Visel, Ray M. Whitlock, Paul E. Wohnoutka, Crissa K. Wolkey, Victoria Y. Wong,

- Matthew Wood, Murat B. Yaylaoglu, Rob C. Young, Brian L. Youngstrom, Xu Feng Yuan, Bin Zhang, Theresa A. Zwingman, and Allan R. Jones. Genome-wide atlas of gene expression in the adult mouse brain. *Nature*, 445(7124):168–176, December 2006. doi: 10.1038/nature05453. URL <https://doi.org/10.1038/nature05453>.
- [18] Horea-Ioan Ioanas, Tina Segessemann, and Markus Rudin. “Mouse Brain Atlases” generator workflows, January 2019. URL <https://doi.org/10.5281/zenodo.2545838>.
- [19] Horea-Ioan Ioanas and Markus Rudin. Reproducible self-publishing for Python-based research. EuroSciPy, August 2018. doi: 10.6084/m9.figshare.7247339.v1. URL https://figshare.com/articles/Reproducible_Self-Publishing_for_Python-Based_Research/7247339.
- [20] Oscar Esteban, Christopher Markiewicz, Ross W Blair, Craig Moodie, Ayse Ilkay Isik, Asier Erramuzpe Aliaga, James Kent, Mathias Goncalves, Elizabeth DuPre, Madeleine Snyder, et al. FMRIPrep: a robust preprocessing pipeline for functional MRI. *Nature Methods*, page 111–116, December 2019. doi: 10.1038/s41592-018-0235-4. URL <https://doi.org/10.1038/s41592-018-0235-4>.
- [21] Erin K. Molloy, Mary E. Meyerand, and Rasmus M. Birn. The influence of spatial resolution and smoothing on the detectability of resting-state and task fMRI. *NeuroImage*, 86:221–230, February 2014. doi: 10.1016/j.neuroimage.2013.09.001. URL <https://doi.org/10.1016/j.neuroimage.2013.09.001>.
- [22] Horea-Ioan Ioanas and Markus Rudin. BIDS Data for “An Optimized Registration Workflow and Standard Geometric Space for Small Animal Brain Imaging”, April 2019. URL <https://doi.org/10.5281/zenodo.2651640>.
- [23] Horea-Ioan Ioanas, Markus Marks, Mehmet Fatih Yanik, and Markus Rudin. Source Code for “An Optimized Registration Workflow and Standard Geometric Space for Small Animal Brain Imaging”, April 2019. URL <https://bitbucket.org/TheChymera/irsabi>.
- [24] Seiji Ogawa, Tso-Ming Lee, Asha S. Nayak, and Paul Glynn. Oxygenation-sensitive contrast in magnetic resonance image of rodent brain at high magnetic fields. *Magnetic Resonance in Medicine*, 14(1):68–78, April 1990. doi: 10.1002/mrm.1910140108. URL <https://doi.org/10.1002/mrm.1910140108>.
- [25] John J.A. Marota, C. Ayata, Michael A. Moskowitz, Robert M. Weisskoff, Bruce R. Rosen, and Joseph B. Mandeville. Investigation of the early response to rat forepaw stimulation. *Magnetic Resonance in Medicine*, 41(2):247–252, February 1999. doi: 10.1002/(sici)1522-2594(199902)41:2<247::aid-mrm6>3.0.co;2-u. URL [https://doi.org/10.1002/\(sici\)1522-2594\(199902\)41:2<247::aid-mrm6>3.0.co;2-u](https://doi.org/10.1002/(sici)1522-2594(199902)41:2<247::aid-mrm6>3.0.co;2-u).
- [26] Michael M Scott, Christi J Wylie, Jessica K Lerch, Roxanne Murphy, Katherine Lobur, Stefan Herlitze, Weihong Jiang, Ron A Conlon, Ben W Strowbridge, and Evan S Deneris. A genetic approach to access serotonin neurons for in vivo and in vitro studies. *Proceedings of the National Academy of Sciences of the United States of America*, 102:16472–16477, November 2005. ISSN 0027-8424. doi: 10.1073/pnas.0504510102. URL <https://doi.org/10.1073/pnas.0504510102>.
- [27] Joanes Grandjean, Alberto Corcobba, Martin C. Kahn, A. Louise Upton, Evan S. Deneris, Erich Seifritz, Fritjof Helmchen, Edward O. Mann, Markus Rudin, and Bechara J. Saab. A brain-wide functional map of the serotonergic responses to acute stress and fluoxetine. *Nature Communications*, 10(1), January 2019. doi: 10.1038/s41467-018-08256-w. URL <https://doi.org/10.1038/s41467-018-08256-w>.
- [28] Anders Eklund, Thomas E Nichols, and Hans Knutsson. Cluster failure: why fMRI inferences for spatial extent have inflated false-positive rates. *Proceedings of the National Academy of Sciences*, page 201602413, June 2016. doi: 10.1073/pnas.1602413113. URL <https://doi.org/10.1073/pnas.1602413113>.
- [29] Robert W Cox. AFNI: software for analysis and visualization of functional magnetic resonance neuroimages. *Computers and Biomedical research*, 29(3):162–173, June 1996. doi: 10.1006/cbmr.1996.0014. URL <https://www.sciencedirect.com/science/article/pii/S0010480996900142>.
- [30] Robert W Cox, Gang Chen, Daniel R Glen, Richard C Reynolds, and Paul A Taylor. FMRI clustering in AFNI: false-positive rates redux. *Brain connectivity*, 7(3):152–171, April 2017. doi: 10.1089/brain.2016.0475. URL <https://doi.org/10.1089/brain.2016.0475>.
- [31] Krzysztof Gorgolewski, Christopher D. Burns, Dav Madison, Cindeeand Clark, Yaroslav O. Halchenko, Michael L. Waskom, and Satrajit S. Ghosh. Nipype: A flexible, lightweight and extensible neuroimaging data processing framework in Python. *Front. Neuroinform.*, 5, 2011. ISSN 1662-5196. doi: 10.3389/

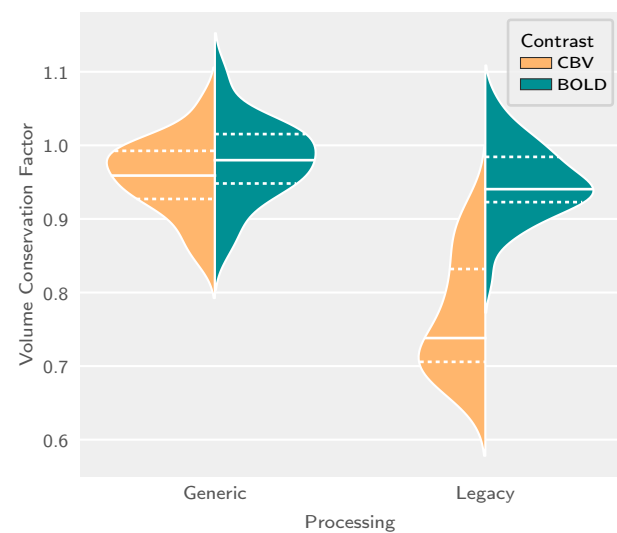
fninf.2011.00013. URL <http://dx.doi.org/10.3389/fninf.2011.00013>.

- [32] Krzysztof J Gorgolewski, Tibor Auer, Vince D Calhoun, R Cameron Craddock, Samir Das, Eugene P Duff, Guillaume Flandin, Satrajit S Ghosh, Tristan Glatard, Yaroslav O Halchenko, et al. The brain imaging data structure, a format for organizing and describing outputs of neuroimaging experiments. *Scientific Data*, 3: 160044, June 2016. doi: 10.1038/sdata.2016.44. URL <https://doi.org/10.1038/sdata.2016.44>.

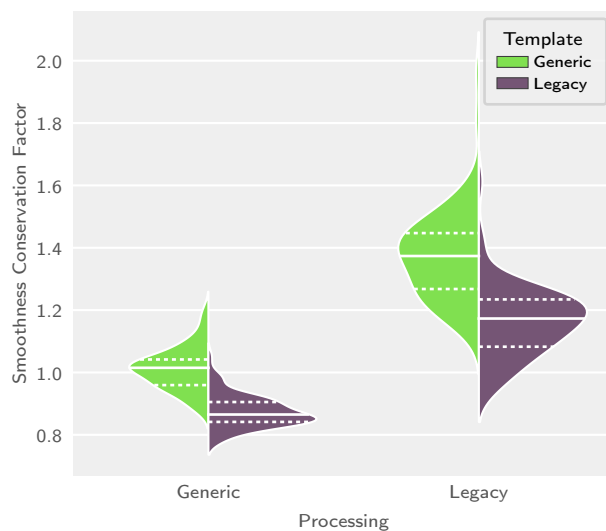
An Optimized Registration Workflow and Standard Geometric Space for Small Animal Brain Imaging



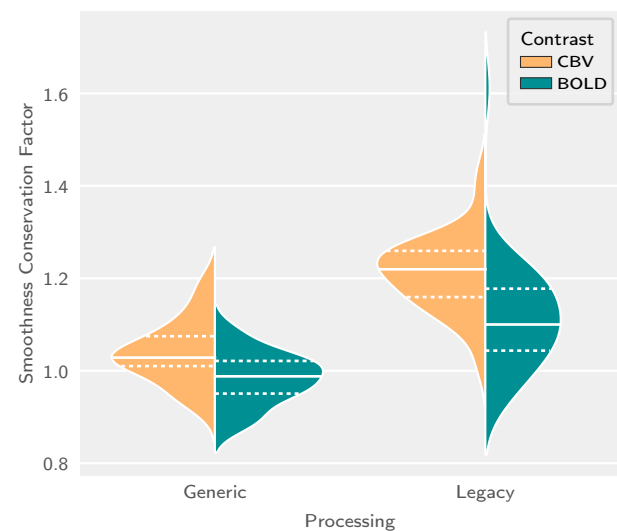
(a) Comparison across workflows and target templates, considering both BOLD and CBV functional contrasts.



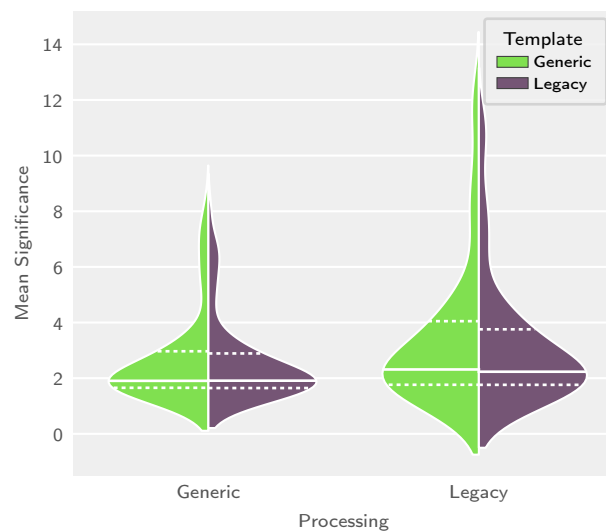
(b) Comparison across workflows and functional contrasts, considering only matching template-workflow combinations.



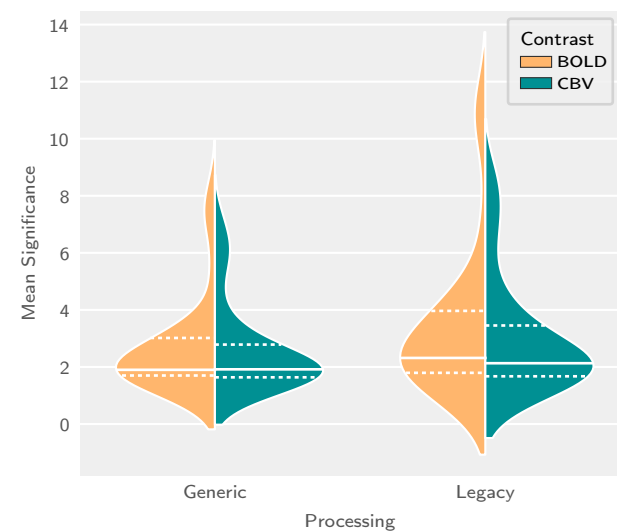
(c) Comparison across workflows and target templates, considering both BOLD and CBV functional contrasts.



(d) Comparison across workflows and functional contrasts, considering only matching template-workflow combinations.

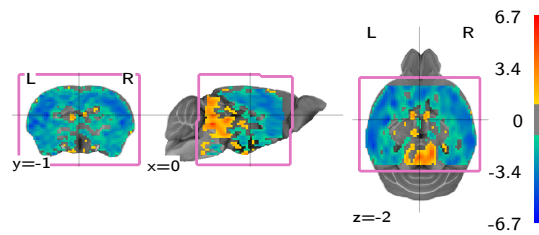


(e) Comparison across workflows and target templates, considering both BOLD and CBV functional contrasts.

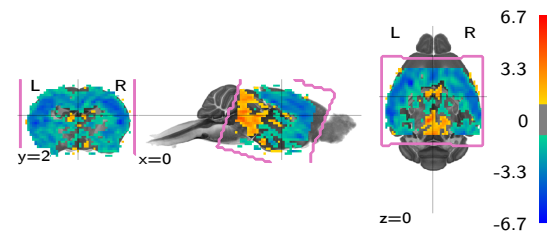


(f) Comparison across workflows and functional contrasts, considering only matching template-workflow combinations.

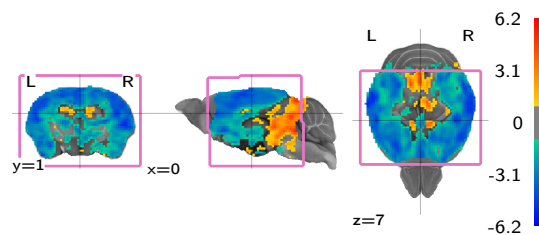
Figure 3: The SAMRI Generic workflow and template optimally and reliably conserve volume and smoothness — unlike the Legacy workflow and template. Plots of three target metrics, with coloured patch widths estimating distribution density, solid lines indicating the sample mean, and dashed lines indicate the inner quartiles.



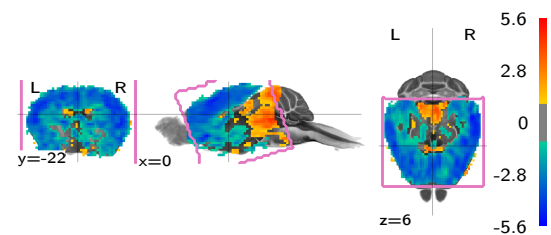
(a) Generic workflow with Generic template CBV map, showing correct slice orientation and coverage correctly bounded to the acquisition area.



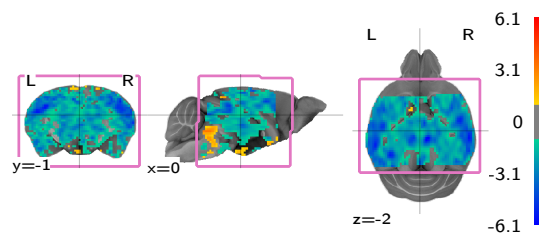
(b) Generic workflow with Legacy template CBV map, showing incorrect slice orientation and coverage correctly bounded to the acquisition area.



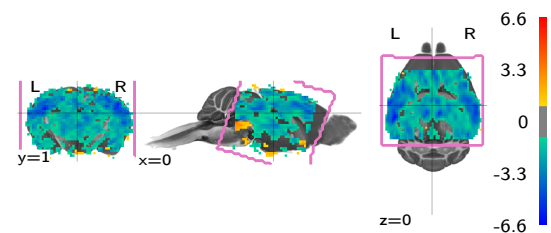
(c) Legacy workflow with Generic template CBV map, showing correct slice orientation and coverage caudally extending beyond the acquisition area.



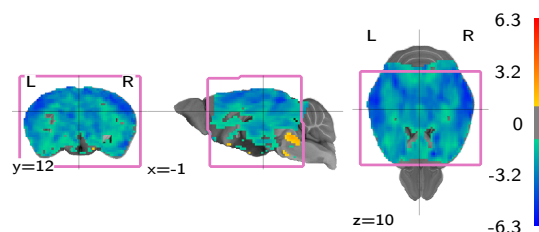
(d) Legacy workflow with Legacy template CBV map, showing incorrect slice orientation and coverage both caudally and rostrally extending beyond acquisition area.



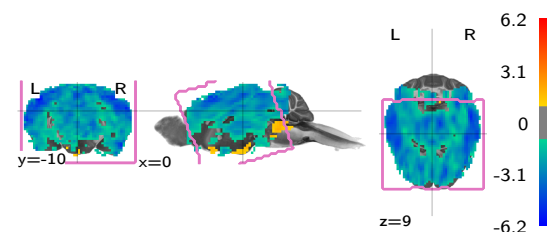
(e) Generic workflow with Generic template BOLD map, showing correct slice orientation and coverage correctly bounded to the acquisition area.



(f) Generic workflow with Legacy template BOLD map, showing incorrect slice orientation and coverage correctly bounded to the acquisition area.



(g) Legacy workflow with Generic template BOLD map, showing correct slice orientation and coverage caudally extending beyond acquisition area.



(h) Legacy workflow with Legacy template BOLD map, showing incorrect slice orientation and coverage both caudally and rostrally extending beyond acquisition area.

Figure 4: Legacy workflow processing leads to a problematic overflow of the statistic maps into adjacent anatomical regions, leaking beyond the acquisition area. SAMRI mitigates this effect as illustrated by multiplanar depictions of second-level omnibus statistic maps separately evaluating CBV and BOLD scans, and thresholded at $|t| \geq 2$. The acquisition area is bracketed in pink, and in comparing it to statistic coverage it is important to note that the latter is always underestimated, as the omnibus statistic contrast is only defined for voxels captured in every evaluated scan.

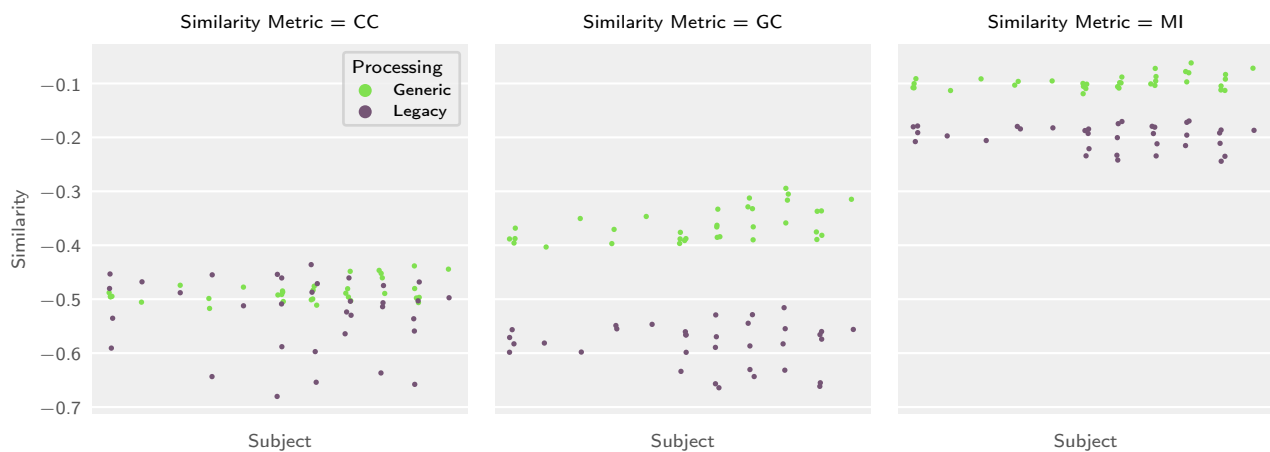
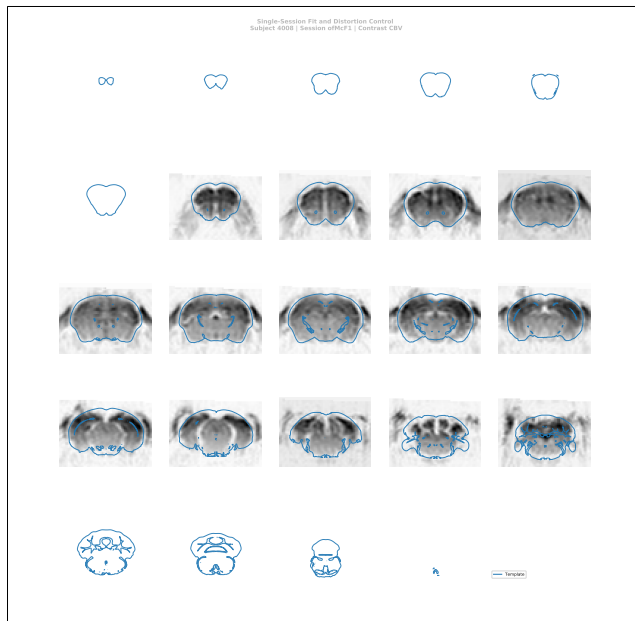


Figure 5: The SAMRI Generic workflow conserves subject-wise variability and minimizes trial-to-trial variability compared to the Legacy workflow. Swarmplots illustrate similarity metric scores of preprocessed images with respect to the corresponding workflow template, plotted across subjects (separated into x-axis bins) and sessions (individual points in each x-axis bin), for the CBV contrast.

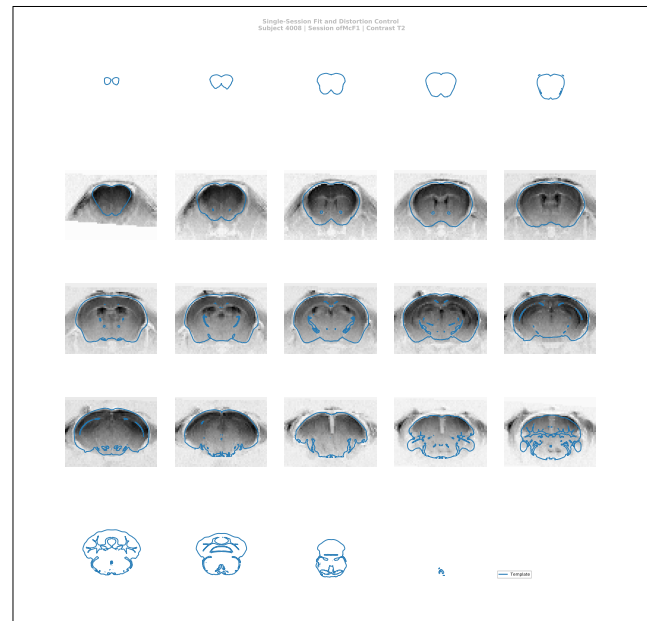
Supplementary Materials

Onset [s]	Duration [s]	Frequency [Hz]	Pulse Width [s]	Wavelength [nm]
222.0	20.0	20.0	0.005	488.0
402.0	20.0	20.0	0.005	488.0
582.0	20.0	20.0	0.005	488.0
762.0	20.0	20.0	0.005	488.0
942.0	20.0	20.0	0.005	488.0
1122.0	20.0	20.0	0.005	488.0

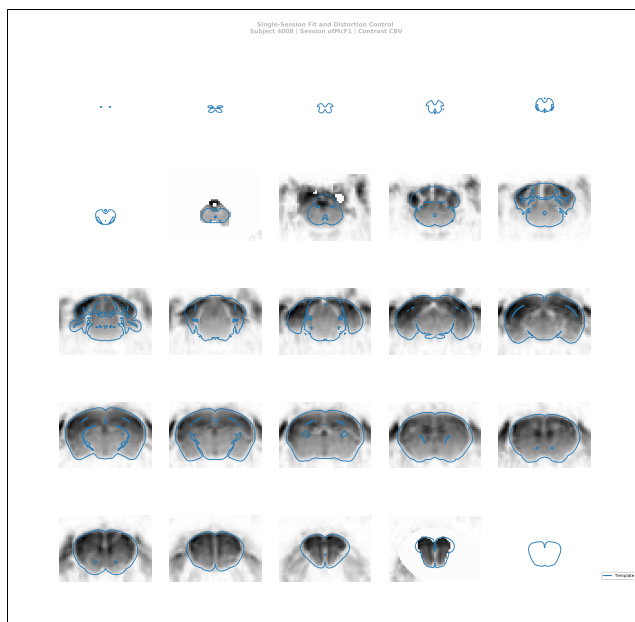
Table S1: Stimulation protocol, as delivered during functional scans. Stimulus event spacing and parameters are constant across scans, but the exact onset time is variable in the 10 s magnitude range due to scanner adjustment time variability.



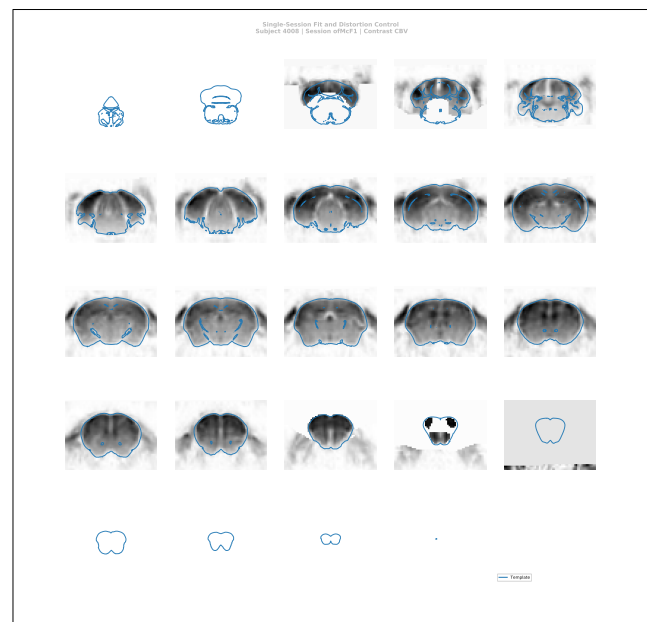
(a) SAMRI Generic workflow with Generic template, note the undistorted mapping and conservative smoothing.



(b) SAMRI Generic workflow with Generic template, inspecting the structural scan intermediary; note the undistorted mapping and conservative smoothing.



(c) SAMRI Legacy workflow with Legacy template, note the strong smoothing and the mapping distortion in the rostral and caudal areas.

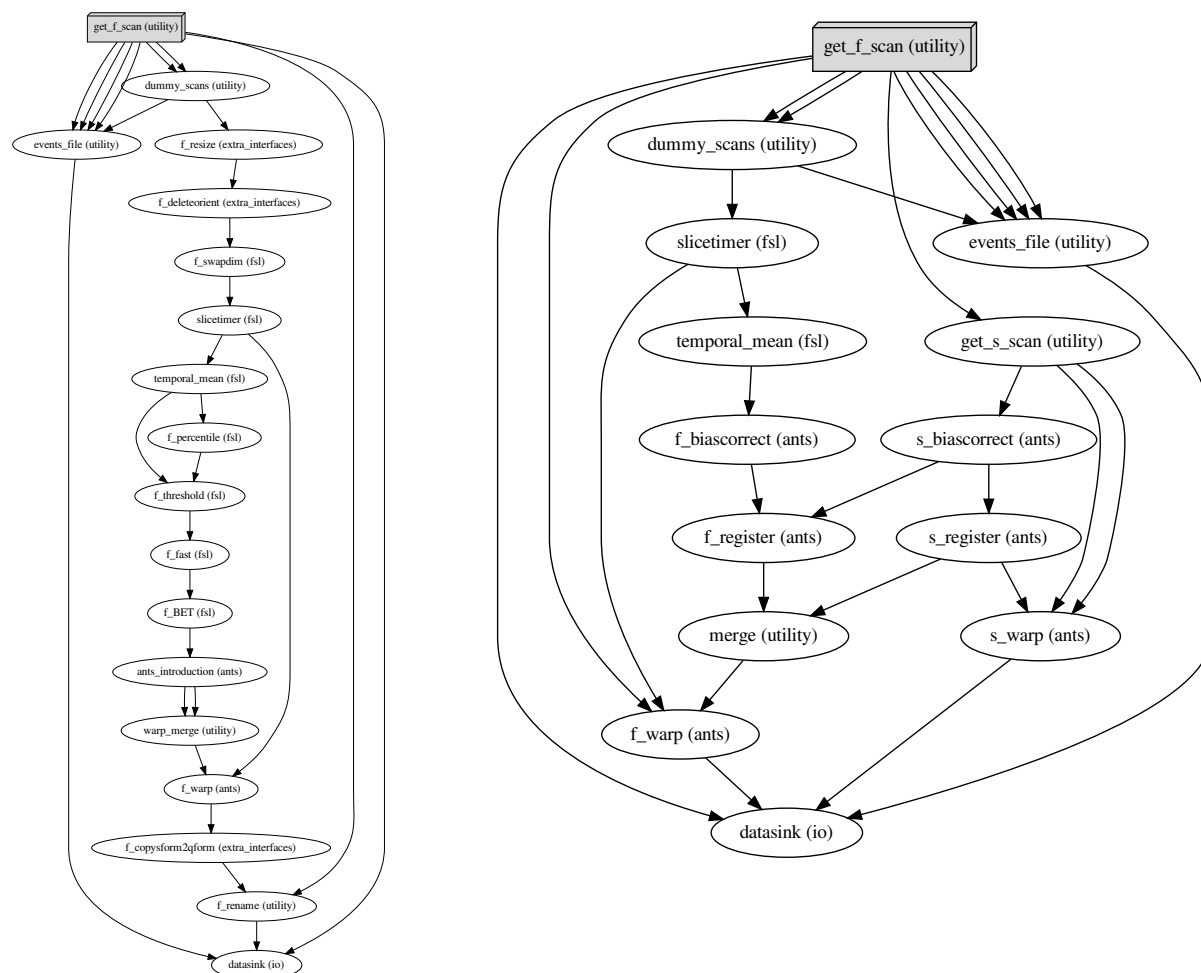


(d) SAMRI Legacy workflow with Generic template, note the strong smoothing and the mapping distortion in the rostral and caudal areas.

Figure S1: The SAMRI Generic workflow induces less smoothness, and provides more accurate coverage. Depicted are automatically created operator overview graphics, which allow a slice-by-slice (spacing analogous to acquisition) inspection of the registration fit. This representation affords a particularly detailed view of the preprocessed MRI data, and highly accurate template contours.



Figure S2: The SAMRI Generic workflow consistently maps high-salience features such as the implant site across sessions. Automatically created operator overview graphic, allowing a slice-by-slice (spacing analogous to acquisition) inspection of registration coherence. This representation permits a coarse assessment of registration consistency for multiple sessions — though at the cost of some clarity. Particularly, this visualization, allows an operator to track the position of high-amplitude fixed features across scans in order to ascertain coherence (similarly to what is automatically assessed by the Variance analysis of the session factor).



(a) “SAMRI Legacy” workflow, which is based on the `antsIntroduction.sh` function (and other functions with hard-coded parameters optimized for human brain registration), and also performs destructive affine manipulations.

(b) “SAMRI Generic” workflow, based on the `antsRegistration` function. The pipeline uses a higher-resolution structural scan intermediary for registration (note the two processing streams), which facilitates differential handling of anatomical variation and susceptibility artefacts. The function used is highly parameterized, and both of its instances — “`s_register`” and “`f_register`” — are supplied in the workflow with defaults optimized for mouse brain registration.

Figure S3: Directed acyclic graphs detailing the precise node names (as seen in the SAMRI source code) for the two alternate MRI registration workflows. The package correspondence of each processing node is appended in parentheses to the node name. The “utility” indication corresponds to nodes based on Python functions specific to the workflow, distributed alongside it, and dynamically wrapped via Nipype. The “extra_interfaces” indication corresponds to nodes using explicitly defined Nipype-style interfaces, which are specific to the workflow and distributed alongside it.